APL Materials

Ferroelectric properties of ion-irradiated bismuth ferrite layers grown via molecular-beam epitaxy

Cite as: APL Mater. **7**, 111101 (2019); https://doi.org/10.1063/1.5125809
Submitted: 27 August 2019 . Accepted: 10 October 2019 . Published Online: 01 November 2019

Antonio B. Mei, Sahar Saremi, Ludi Miao, Matthew Barone, Yongjian Tang, Cyrus Zeledon, Jürgen Schubert, Daniel C. Ralph, Lane W. Martin, and Darrell G. Schlom

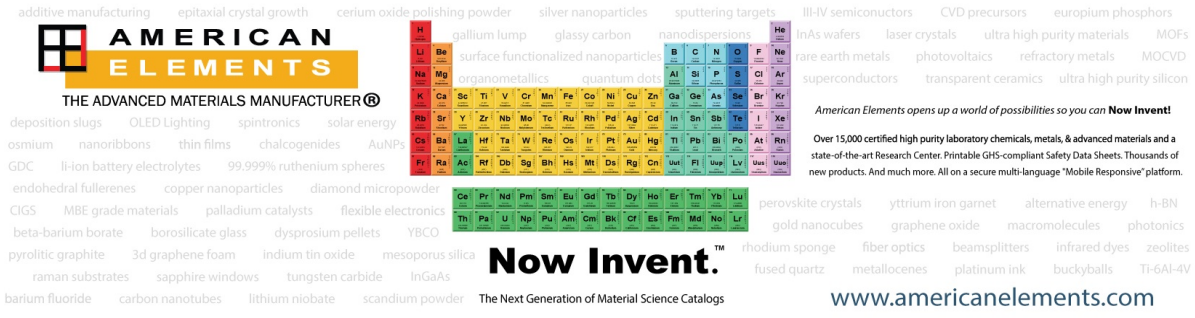

Ferroelectric properties of ion-irradiated bismuth ferrite layers grown via molecular-beam epitaxy

Cite as: APL Mater. 7, 111101 (2019); doi: 10.1063/1.5125809
Submitted: 27 August 2019 • Accepted: 10 October 2019 •
Published Online: 1 November 2019

Antonio B. Mei,[1,a)] Sahar Saremi,[2] Ludi Miao,[3] Matthew Barone,[1] Yongjian Tang,[4] Cyrus Zeledon,[1] Jürgen Schubert,[5] Daniel C. Ralph,[4,6] Lane W. Martin,[2,7] and Darrell G. Schlom[1,6]

AFFILIATIONS

[1]Department of Materials Science and Engineering, Cornell University, Ithaca, New York 14853, USA
[2]Department of Materials Science and Engineering, University of California, Berkeley, Berkeley, California 94720, USA
[3]Laboratory of Atomic and Solid State Physics, Cornell University, Ithaca, New York 14853, USA
[4]Physics Department, Cornell University, Ithaca, New York 14853, USA
[5]Peter Grünberg Institute (PGI-9) and JARA-Fundamentals of Future Information Technology, Forschungszentrum Jülich GmbH, 52425 Jülich, Germany
[6]Kavli Institute at Cornell for Nanoscale Science, Ithaca, New York 14853, USA
[7]Materials Sciences Division, Lawrence Berkeley National Laboratory, Berkeley, California 94720, USA

[a)]amei2@illinois.edu

ABSTRACT

We systematically investigate the role of defects, introduced by varying synthesis conditions and by carrying out ion irradiation treatments, on the structural and ferroelectric properties of commensurately strained bismuth ferrite $Bi_xFe_{2-x}O_3$ layers grown on $SrRuO_3$-coated $DyScO_3(110)_o$ substrates using adsorption-controlled ozone molecular-beam epitaxy. Our findings highlight ion irradiation as an effective approach for reducing through-layer electrical leakage, a necessary condition for the development of reliable ferroelectrics-based electronics.

I. INTRODUCTION

$BiFeO_3$ crystalizes in a rhombohedrally distorted perovskite structure (space group #161, *R3c*) and exhibits the combination of ferroelectricity and spin-canted weak ferromagnetism.[1–3] At room temperature, the polar and magnetic order parameters are coupled. As a result, when ferroelectric domains are poled, magnetic moments reorient deterministically.[2,4,5] Voltage-controlled magnetism is important for enabling low-power spintronic devices that operate efficiently and independently of current-based switching mechanisms, including Oersted induction and spin-transfer torque.[6] Utilizing $BiFeO_3$ for practical voltage-controlled spintronics, however, requires overcoming reliability challenges currently limiting ferroelectric-based devices.[7] Key among these is reducing through-film leakage.[8–10]

In this letter, we investigate the influence of growth conditions and postdeposition ion-irradiation treatments on the composition, structure, and ferroelectric properties of epitaxial $Bi_xFe_{2-x}O_3$ layers grown via adsorption-controlled ozone molecular-beam epitaxy. Structural characterization reveals that stoichiometric films, for which bismuth and iron concentrations are equal (i.e., $x \approx 1.00$), exhibit the highest crystalline and ferroelectric domain perfection. The leakage characteristics of these high-quality layers are found to be similar to defective layers grown near the single-phase field boundaries (i.e., $x \neq 1.00$). Through film leakage is dramatically reduced by irradiating both stoichiometric and nonstoichiometric samples with He^+ ions.

II. FILM GROWTH

$Bi_xFe_{2-x}O_3$ layers are grown to a thickness of ≃200 nm on $SrRuO_3$-coated $(110)_o$-oriented $DyScO_3$ substrates (*o* subscripts denote orthorhombic indices in the nonstandard *Pbnm* setting) via adsorption-controlled molecular-beam epitaxy in a Veeco GEN10

system (base pressure $P_{Base} = 1 \times 10^{-8}$ Torr = 1.3×10^{-6} Pa). $SrRuO_3$ is selected as an epitaxial bottom electrode[11] due to its relatively low electrical resistivity (170 $\mu\Omega$-cm at room temperature)[12] and lattice match with the $DyScO_3$ substrate (lattice mismatch $m = 0.6\%$). The $SrRuO_3$ electrodes are deposited as described in Refs. 12 and 13 to thicknesses of ≃20 nm. $Bi_xFe_{2-x}O_3$ films are grown subsequently without breaking vacuum at growth temperatures T_s between 550 °C and 650 °C, estimated using a thermocouple in indirect contact with the growth surface.

Iron (99.995% pure) and bismuth (99.9999% pure) are simultaneously[14] supplied to the growth surface from effusion cells operating at temperatures near 1250 °C and 650 °C, respectively. Iron fluxes are fixed at $J_{Fe} = 2.4 \times 10^{13}$ cm^{-2} s^{-1}, yielding bismuth ferrite deposition rates of 1.1 nm/min; bismuth fluxes are varied between $J_{Bi} = 4.8 \times 10^{13}$ cm^{-2} s^{-1}and 38.4×10^{13} cm^{-2} s^{-1}, corresponding to J_{Bi}/J_{Fe} flux ratios spanning 2 through 16. High bismuth fluxes ($J_{Bi}/J_{Fe} \gg 1$) promote the incorporation of bismuth into the growing film, compensating for the desorption of volatile BiO_x species.[15]

Elemental oxygen is supplied via atmospheric mixtures consisting of 20% O_2 and 80% O_3. The deposition pressure is maintained at 1×10^{-5} Torr (1.3×10^{-3} Pa), corresponding to an equivalent[16,17] ozone flux of $J_{O_3} \approx 10^{16}$ cm^{-2} s^{-1}. The use of strong oxidants[18,12,19] and high ozone fluxes ($J_{O_3}/J_{Fe} \approx 500$) suppress the formation of oxygen vacancies, which engender mobile electrons.[20]

A. Structure and composition

Initial film growth experiments focus on determining the effects of incident flux ratios $2 \le J_{Bi}/J_{Fe} \le 16$ and deposition temperatures 550 °C ≤ T_s ≤ 650 °C on the composition and structure of the $Bi_xFe_{2-x}O_3$ layers grown on $SrRuO_3/DyScO_3(110)_o$.

Figure 1(a) is a variability chart[21] showing film bismuth fractions x determined from $Bi_xFe_{2-x}O_3$ layers using Rutherford backscattering spectrometry.[22–24] Measured x values span 0.90 ($J_{Bi}/J_{Fe} = 4$, $T_s = 650$ °C) through 1.05 ($J_{Bi}/J_{Fe} = 16$, $T_s = 600$ °C). Increasing T_s and reducing J_{Bi}/J_{Fe} result in lower film bismuth fractions x; in particular, we find that a 50 °C increase in T_s has an effect on x equivalent to a two-fold reduction in J_{Bi}/J_{Fe}. The loss of bismuth at higher temperatures results from thermally activated BiO_x desorption.[25–27]

The phase composition and structural perfection of as-deposited films are investigated using x-ray diffraction (XRD) θ-2θ scans and reciprocal space maps (RSM). The findings are summarized as a function of incident metal flux ratios J_{Bi}/J_{Fe} and deposition temperatures T_s in Fig. 1(b). Three structurally distinct growth regions are observed, comprised of phase-pure $Bi_xFe_{2-x}O_3$ layers [white region, Fig. 1(b)] as well as two mixed-phase $Bi_xFe_{2-x}O_3$ regions, one with Fe_2O_3 inclusions and the other with $Bi_2O_{2.5}$ precipitates [blue and red regions, Fig. 1(b)]. The single-phase regime spans a wide temperature window in excess of 100 °C, which has been modeled kinetically and shown to narrow rapidly with decreasing oxidant pressures.[15] Together with film compositional measurements [Fig. 1(a)], a single-phase-field width spanning $x = 0.90$–1.05 is established, in close agreement with prior reports for layers grown via pulsed-laser deposition.[28] Within the single-phase field, RSMs performed about symmetric film reflections reveal two categorically distinct peak shapes [Fig. 1(b) insets]: at lower

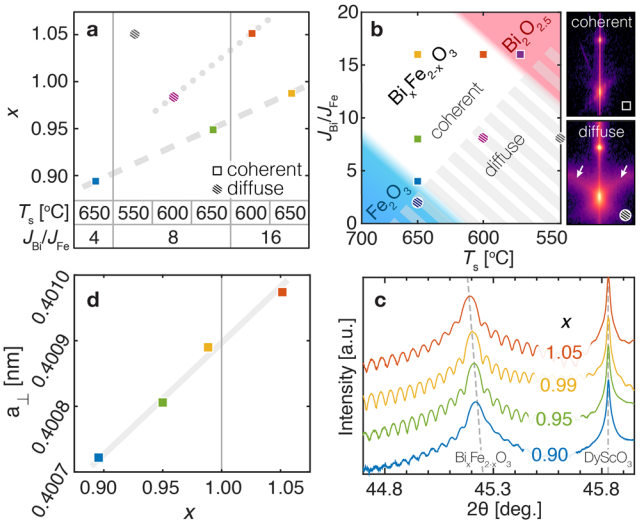

FIG. 1. Composition and structure of epitaxial $Bi_xFe_{2-x}O_3/SrRuO_3/DyScO_3(110)_o$ heterostructures. (a) Variability chart showing film bismuth fractions x vs incident metal flux ratios J_{Bi}/J_{Fe} and deposition temperatures T_s. The broken lines connect points grown at the same temperature T_s. Diffuse and coherent labels refer to RSM peak shapes [see the inset in (b)]. (b) J_{Bi}/J_{Fe} vs T_s parameter space governing the adsorption-controlled growth of $Bi_xFe_{2-x}O_3$ layers via ozone molecular-beam epitaxy. White regions denote phase-pure layers; blue and red areas indicate mixed-phase films with Fe_2O_3 and $Bi_2O_{2.5}$ inclusions, respectively; striped (non-striped) regions identify regimes where RSMs carried out about $Bi_xFe_{2-x}O_3$ 002_p reflections (inset) display diffuse (coherent) peak shapes. The dimensions of the RSMs are 0.08×0.13 nm^{-2}. (c) XRD θ-2θ diffracted intensities near 002_p film and substrate reflections from $Bi_xFe_{2-x}O_3$ layers. (d) Corresponding film out-of-plane lattice parameters $a_\perp$ vs bismuth fractions x.

deposition temperatures and bismuth fluxes, the fundamental film reflections display diffuse features; at higher T_s and J_{Bi}/J_{Fe} values, the peaks exhibit coherent profiles. In the remainder of this letter, we focus on the latter set of films, for which the structural quality is superior.

Figure 1(c) shows diffracted θ-2θ x-ray intensities collected near 002_p film and substrate peaks from $Bi_xFe_{2-x}O_3$ layers (p subscripts denotes pseudocubic indices) grown along the isoflux $J_{Bi}/J_{Fe} = 16$ and isotherm $T_s = 650$ °C lines. As the film bismuth fraction x is increased, film reflections shift to slightly lower 2θ values, resulting in out-of-plane lattice parameter values $a_\perp$ which grow linearly with composition x [Fig. 1(d)].[29] The variation in $a_\perp$ values suggests a changing concentration of point defects within the films.

B. Surface and domain morphology

The combination of reflection high-energy electron diffraction (RHEED) and atomic force microscopy (AFM) is employed to investigate the surface morphology of epitaxial $Bi_xFe_{2-x}O_3$ layers deposited on $SrRuO_3$-coated $DyScO_3(110)_o$ substrates. Figures 2(a)–2(j) are *in situ* RHEED patterns collected along $\langle 100 \rangle_p$ and $\langle 110 \rangle_p$ azimuths as a function of film bismuth fractions x between 0.90 and 1.07; corresponding *ex situ* AFM topography maps are shown in Figs. 2(k)–2(o).

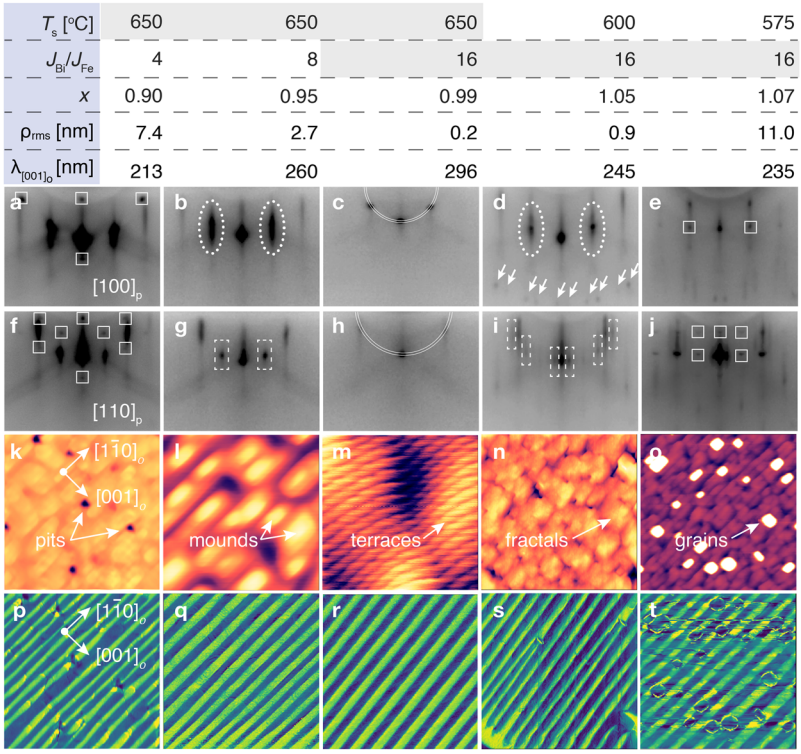

FIG. 2. Surface and domain morphology of epitaxial $Bi_xFe_{2-x}O_3$ layers grown on $SrRuO_3$-coated $DyScO_3(110)_o$ substrates. *In situ* RHEED patterns viewed along (a)–(e) $\langle 100\rangle_p$ and (f)–(j) $\langle 110\rangle_p$ azimuths together with *ex situ* (k)–(o) AFM topography maps and (p)–(t) lateral PFM images. Each column of panels corresponds to an individual sample. The first five rows indicate growth flux ratios J_{Bi}/J_{Fe}, deposition temperatures T_s, film bismuth fractions x, surface roughness values ρ_{rms}, and domain periodicities $\lambda_{[001]_o}$. In (a)–(j), arrows designate Kikuchi lines, solid squares identify bulk diffraction spots, dotted ovals denote streaked reflections, dashed rectangles indicate surface reconstructions, and double arcs demarcate specular reflections. Films with the highest structural perfection, smoothest surface, and most well-ordered domain morphologies are obtained near stoichiometry for $x = 0.99$. (k)–(t) are each $3 \times 3\ \mu m^2$.

Stoichiometric $Bi_xFe_{2-x}O_3$ layers with $x = 0.99$ exhibit electron reflection patterns characterized by circular spots. The spots lie on half-circles [double arcs, Figs. 2(c) and 2(h)] on which the specular condition is satisfied. Both the position and shape of the spots indicate two-dimensional step-flow growth[30]—a conclusion which is corroborated by AFM height maps [e.g., Fig. 2(m)], which consist of atomically smooth surfaces (root-mean-square surface fluctuations $\rho_{rms} = 0.2$ nm) with well-defined terraces and unit-cell-tall step edges.

Increasing x to 1.05 causes the reflected spots to elongate vertically into streaked ellipses [ovals, Fig. 2(d)]. Concurrently, sixth-order stripes [rectangles, Fig. 2(i)] as well as split Kikuchi lines [arrows, Fig. 2(d)] also appear. Together, these features suggest reconstructions of surface atoms and broadening of surface widths following the formation of mosaic blocks.[31,32] Surface topographies are determined via AFM [Fig. 2(n)] to consist of shallow fractal-like features,[33] yielding a surface roughness of $\rho_{rms} = 0.9$ nm.

For higher bismuth fractions of $x = 1.07$, arrays of bulk diffraction spots are observed [squares, Figs. 2(e) and 2(j)]. Bulk diffraction is a hallmark of three-dimensional growth[34] and occurs when glancing electrons penetrate through surface protrusions.[35] Such features are visible in AFM height images, including Fig. 2(o), and are attributed to $Bi_2O_{2.5}$ grains.[26] The protrusions also lead to rough surfaces for which $\rho_{rms} = 11.0$ nm, exceeding the roughness values obtained here for stoichiometric bismuth ferrite layers by over an order of magnitude.

Systematic changes in the morphologies of the layers are also observed for bismuth-deficient layers. RHEED and AFM images collected from $Bi_xFe_{2-x}O_3$ films with $x = 0.95$ exhibit half-order spots [rectangles, Fig. 2(g)] indicating doubling of surface unit cells and shallow islands characteristic of the layer-by-layer growth in the presence of limited adatom diffusivity across step-edge barriers[36,37] [Fig. 2(l)]. For films with $x = 0.90$, bulk diffraction spots are detected in RHEED patterns [squares, Figs. 2(a) and 2(f)] and pits are observed in AFM height maps [Fig. 2(k)]. The surface roughness for bismuth deficient layers spans $\rho_{rms} = 2.7$ nm ($x = 0.95$) through 7.4 nm ($x = 0.90$).

Collectively, the direct- and Fourier-space analyses establish a rich morphological phase diagram in which topographical features vary systematically and depend sensitively on film composition. This makes RHEED a sensitive *in situ* monitor for characterizing the growth of $Bi_xFe_{2-x}O_3$ layers in real time.

C. Ferroelectric properties

Figures 2(p)–2(t) are lateral piezoforce microscopy (PFM) images showing ferroelectric domain morphologies of $Bi_xFe_{2-x}O_3$ layers grown as a function of the film bismuth fraction x. Stoichiometric layers with $x = 0.99$ exhibit bimodal contrast variations corresponding to two ferroelectric domain variants [Fig. 2(r)], in agreement with prior reports.[13] The domains assemble into one-dimensional stripes with remarkable long-range order and an in-plane periodicity along $[001]_o$ of $\lambda_{[001]_p} = 296 \pm 20$ nm. Increasing x to 1.05 and 1.07 progressively disrupts the uniformity of the stripe pattern. Concurrently, array periodicities decrease to $\lambda_{[001]_o} = 245 \pm 32$ ($x = 1.05$) and 235 ± 44 nm ($x = 1.07$). Increased disorder and reduced domain widths are also observed with decreasing x in bismuth deficient layers; in these cases, $\lambda_{[001]_o} = 260 \pm 38$

(x = 0.95) and 213 ± 42 nm (x = 0.90). Because of the increased pattern disorder observed near the single-phase field boundary, we hypothesize that pattern irregularities are due to lattice imperfections, including the cluster of point defects which accommodate film nonstoichiometry. The varying domain periods reflect an interplay between polar stiffness and depolarization effects.[38–41] Near x = 0.99, polar stiffness reduces domain wall densities by penalizing the regions containing rapidly varying polarization. Conversely, near the single-phase field boundaries, depolarization effects dominate, suppressing stray fields by bringing domain walls closer together.

The ferroelectric properties of the $Bi_xFe_{2-x}O_3$ films are quantified using metal-ferroelectric-metal capacitor structures. Platinum top electrodes, in the form of 40-μm-diameter circles, are defined lithographically. Polarization P vs electric field E measurements are performed by applying trains of bipolar triangular pulses to the devices at a frequency of 10 kHz using a Precision Multiferroic Tester (Radiant Technologies, Inc.).

In the as-deposited state, the films display pronounced leakage which impede ferroelectric poling. Leakage in bismuth ferrite arises from a combination of factors, including domain-wall conductivity[42] as well as electron and hole donor defects such as oxygen vacancies[20] and Fe^{2+}-based complexes.[43] Ion irradiation was recently demonstrated as a successful avenue for increasing the resistivity of leaky ferroelectrics.[44,45] We adopt a similar strategy and bombard our patterned structures with 3.0 MeV He^{2+} ions. At this energy, the ions penetrate to a mean depth of ~15 μm, damaging the film lattice but preserving the film chemistry.

Figure 3(a) shows $P(E)$ curves obtained as a function of irradiation doses D between 0.3×10^{15} and 1×10^{16}/cm^2 from a stoichiometric $Bi_xFe_{2-x}O_3$ film grown with x = 0.99. In contrast to $P(E)$ curves measured from as-deposited heterostructures [for reference, also shown in Fig. 3(a)], devices irradiated with $D \geq 0.3 \times 10^{15}$/cm^2 exhibit clear signatures of ferroelectricity, manifested in the form of hysteresis loops. For $0.3 \times 10^{15} \leq D \leq 1 \times 10^{15}$/cm^2, small residual leakage causes the hysteresis loop to be open, but increasing D further causes the loops to close completely, reflecting progressively decreased leakage. The suppression of leakage in irradiated layers is attribute to the formation of carrier scattering and trapping defects.[45]

Figure 3(a) also demonstrates that, as irradiation doses are increased, ferroelectric coercive fields grow from E_c = 0.15 MV/cm (D = 0.3×10^{15}/cm^2) to 0.90 MV/cm (1×10^{16}/cm^2), following the exponential relationship $E_c = 0.14e^{0.19D}$ (here, the units for E_c and D are MV/cm and 10^{15}/cm^2, respectively). Measured E_c values are comparable to those reported for epitaxial $BiFeO_3$ films deposited on $SrRuO_3/DyScO_3(001)$[45] and $SrTiO_3$:Nb(001)[28] but are larger than the 0.08 MV/cm value obtained for free-standing bismuth ferrite membranes, for which domain walls move unobstructed by epitaxial strain.[46] The larger coercive fields of irradiated devices are attributed to the formation of domain-wall-pinning defects.

Hysteresis loops measured from $Bi_xFe_{2-x}O_3$-based devices[47] bombarded with 3×10^{15} ions/cm^2 are presented as a function of film bismuth fractions x in Fig. 3(c). Remanent polarizations are approximately constant at 62 ± 6 μC/cm^2, independent of the bismuth fraction. This is consistent with a spontaneous polarization of P_s = 107 ± 10 μC/cm^2 along $\langle 111 \rangle_p$, the polarization direction in bismuth ferrite. As x is increased, however, coercive fields E_c vary substantially, decreasing from 0.57 (x = 0.90) to 0.31 MV/cm (x = 0.99) before rising to 0.35 MV/cm (x = 1.05). The reduced E_c values observed near stoichiometry are consistent with the lower defect concentration and higher structural perfection of these films (see Fig. 2).

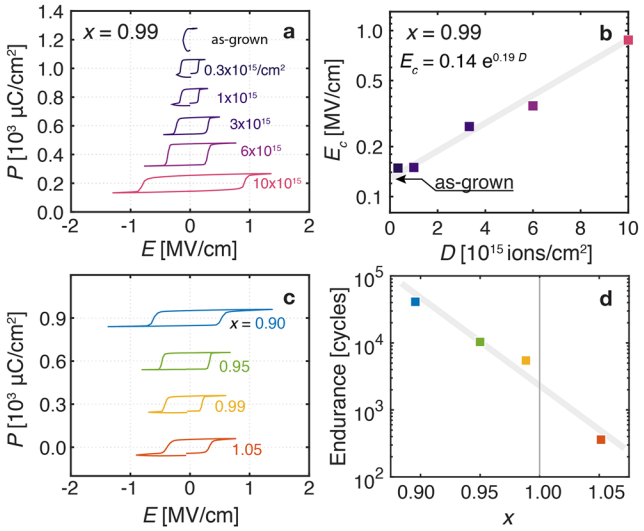

FIG. 3. Ferroelectric properties of Pt/$Bi_xFe_{2-x}O_3$/$SrRuO_3$/$DyScO_3(110)_o$ heterostructures, fabricated with 40-μm-diameter circular platinum top contacts. (a) Polarization P vs electric field E measurements collected from a $Bi_xFe_{2-x}O_3$ film with x = 0.99 irradiated with 3.0 MeV He^{2+} ions as a function of dose D. (b) Coercive field E_c vs irradiation dose D extracted from curves in (a). (c) $P(E)$ hysteresis loops as a function of film bismuth fractions x, measured from samples dosed with 3×10^{15} ions/cm^2. (d) Ferroelectric endurance vs film bismuth fractions x for similarly irradiated samples. Curves in (a) and (c) are vertically offset for clarity.

When cyclically poled, bismuth ferrite layers exhibit fatigue-induced failure. The mechanisms responsible for fatigue are diverse: conducting filaments form causing electrical shorts,[46] charge injection at ferroelectric/electrode interfaces suppresses domain nucleation,[48,49] and pinned domains grow in size.[50] To characterize the endurance of our $Bi_xFe_{2-x}O_3$ layers and determine n, the number of polarization cycles tolerated before breakdown, we employ a 10 kHz rectangular waveform with variable bias amplitudes between ±0.35–0.65 MV/cm to ensure complete poling during testing. Figure 3(d) shows n as a function of the film bismuth fraction x. For bismuth-rich films with x = 1.05, repeated poling leads to breakdown above 3×10^2 cycles. As x is decreased, n grows exponentially to 6×10^3 (x = 0.99) and 4×10^4 (x = 0.90). The observed n values are typical of ferroelectric capacitor structures in which at least one of the electrodes is a metal[51] and can be enhanced by exclusively employing epitaxial conducting oxide electrodes.[52] The combination of oxide electrodes, ion irradiation, and bismuth deficient films thus provides an avenue for prolonging the reliability of $Bi_xFe_{2-x}O_3$ capacitors.

III. CONCLUSIONS

Commensurately strained $Bi_xFe_{2-x}O_3$ layers grown on $SrRuO_3$-coated $DyScO(110)_o$ substrates using adsorption-controlled ozone molecular-beam epitaxy are employed to investigate the role of

defects, introduced by varying synthesis conditions and by performing postgrowth ion bombardment, on the chemical composition, structural characteristics, domain morphology, and ferroelectric attributes of bismuth ferrite. Within the explored ranges of growth temperature 550 °C ≤ T_s ≤ 650 °C and incident bismuth-to-iron flux ratios 2 ≤ J_{Bi}/J_{Fe} ≤ 16, a single-phase field with bismuth fractions x spanning 0.90 through 1.07 is established. The varying film compositions are accompanied by topographical features that include pits (x = 0.90), mounds (x = 0.95), terraces (x ≈ 1.00), fractals (x = 1.05), and protrusions (x = 1.07); each feature produces unique diffraction signatures in RHEED suitable for monitoring film growth in real time.

Film polarization morphologies generally consist of two domain variants arranged in stripe patterns. Pattern perfection and geometry depend sensitively on point defect profiles, with the widest domain widths and most periodic structures occurring near stoichiometry (x ≈ 1.00). In the as-deposited state, all films display excessive leakage which impede ferroelectric poling when tested using fabricated 40-μm-diameter platinum-capped capacitor structures. By performing postgrowth ion irradiation treatments, leakage is suppressed, yielding closed polarization-vs-field hysteresis loops. Remanent polarizations are constant at ~60 μC/cm^2 and independent of film composition; coercive fields are reduced near stoichiometry, where the bismuth and iron concentration are equal. Bismuth deficiency is demonstrated as an avenue for enhancing the endurance of $Bi_xFe_{2-x}O_3$-based ferroelectric devices.

ACKNOWLEDGMENTS

This work was supported in part by the Semiconductor Research Corporation (SRC) as nCORE task 2758.003 and NSF under the E2CDA (Grant No. ECCS-1740136) programs. S.S. acknowledges support from the U.S. Department of Energy, Office of Science, Office of Basic Energy Sciences, Materials Sciences and Engineering Division under Contract No. DE-AC02-05-CH11231 (Materials Project program KC23MP) for the development of ferroelectric thin films and ion-beam-induced defect studies. L.W.M. acknowledges support from the National Science Foundation under Grant No. DMR-1708615. This work made use of the Cornell Center for Materials Research (CCMR) Shared Facilities, which are supported through the NSF MRSEC program (Grant No. DMR-1719875). Substrate preparation was performed in part at the Cornell NanoScale Facility, a member of the National Nanotechnology Coordinated Infrastructure (NNCI), which is supported by the NSF (Grant No. ECCS-1542081).

REFERENCES

[1] J. Wang, J. B. Neaton, H. Zheng, V. Nagarajan, S. B. Ogale, B. Liu, D. Viehland, V. Vaithyanathan, D. G. Schlom, U. V. Waghmare, N. A. Spaldin, K. M. Rabe, M. Wuttig, and R. Ramesh, Science **299**, 1719 (2003).
[2] T. Zhao, A. Scholl, F. Zavaliche, K. Lee, M. Barry, A. Doran, M. P. Cruz, Y. H. Chu, C. Ederer, N. A. Spaldin, R. R. Das, D. M. Kim, S. H. Baek, C. B. Eom, and R. Ramesh, Nat. Mater. **5**, 823 (2006).
[3] I. A. Sergienko and E. Dagotto, Phys. Rev. B **73**, 094434 (2006).
[4] Y.-H. Chu, L. W. Martin, M. B. Holcomb, M. Gajek, S.-J. Han, Q. He, N. Balke, C.-H. Yang, D. Lee, W. Hu, Q. Zhan, P.-L. Yang, A. Fraile-rodríguez, A. Scholl, S. X. Wang, and R. Ramesh, Nat. Mater. **7**, 478 (2008).
[5] J. T. Heron, J. L. Bosse, Q. He, Y. Gao, M. Trassin, L. Ye, J. D. Clarkson, C. Wang, J. Liu, S. Salahuddin, D. C. Ralph, D. G. Schlom, J. Íñiguez, B. D. Huey, and R. Ramesh, Nature **516**, 370 (2014).
[6] J. T. Heron, D. G. Schlom, and R. Ramesh, Appl. Phys. Rev. **1**, 021303 (2014).
[7] S. Fusil, V. Garcia, A. Barthélémy, and M. Bibes, Annu. Rev. Mater. Res. **44**, 91 (2014).
[8] G. W. Pabst, L. W. Martin, Y.-H. Chu, and R. Ramesh, Appl. Phys. Lett. **90**, 072902 (2007).
[9] N. A. Spaldin, S.-W. Cheong, and R. Ramesh, Phys. Today **63**(10), 38 (2010).
[10] M. Lorenz, M. S. Ramachandra Rao, T. Venkatesan, E. Fortunato, P. Barquinha, R. Branquinho, D. Salgueiro, R. Martins, E. Carlos, A. Liu, F. K. Shan, M. Grundmann, H. Boschker, J. Mukherjee, M. Priyadarshini, N. DasGupta, D. J. Rogers, F. H. Teherani, E. V. Sandana, P. Bove, K. Rietwyk, A. Zaban, A. Veziridis, A. Weidenkaff, M. Muralidhar, M. Murakami, S. Abel, J. Fompeyrine, J. Zuniga-Perez, R. Ramesh, N. A. Spaldin, S. Ostanin, V. Borisov, I. Mertig, V. Lazenka, G. Srinivasan, W. Prellier, M. Uchida, M. Kawasaki, R. Pentcheva, P. Gegenwart, F. Miletto Granozio, J. Fontcuberta, and N. Pryds, J. Phys. D: Appl. Phys. **49**, 433001 (2016).
[11] C. B. Eom, R. J. Cava, R. M. Fleming, J. M. Phillips, R. B. vanDover, J. H. Marshall, J. W. P. Hsu, J. J. Krajewski, and W. F. Peck, Science **258**, 1766 (1992).
[12] H. P. Nair, Y. Liu, J. P. Ruf, N. J. Schreiber, S.-L. Shang, D. J. Baek, B. H. Goodge, L. F. Kourkoutis, Z.-K. Liu, K. M. Shen, and D. G. Schlom, APL Mater. **6**, 046101 (2018).
[13] A. B. Mei, Y. Tang, J. Schubert, D. Jena, H. G. Xing, D. C. Ralph, and D. G. Schlom, APL Mater. **7**, 071101 (2019).
[14] J. A. Mundy, C. A. Heikes, B. F. Grosso, D. F. Segedin, Z. Wang, B. H. Goodge, Q. N. Meier, C. T. Nelson, B. Prasad, L. F. Kourkoutis, W. D. Ratcliff, N. A. Spaldin, R. Ramesh, and D. G. Schlom, e-print arXiv:1812.09615 (2018).
[15] E. H. Smith, J. F. Ihlefeld, C. A. Heikes, H. Paik, Y. Nie, C. Adamo, T. Heeg, Z.-K. Liu, and D. G. Schlom, Phys. Rev. Mater. **1**, 023403 (2017).
[16] Conversion between equivalent fluxes J and pressures P are achieved through the relationship $J = P\cos\theta/\sqrt{\pi m k_B T/8}$, in which m and T are molecular mass and temperature, θ is the incident angle of the molecular beam, and k_B is Boltzmann's constant.
[17] C. D. Theis, J. Yeh, D. G. Schlom, M. E. Hawley, and G. W. Brown, Thin Solid Films **325**, 107 (1998).
[18] Ozone is experimentally at least 200× more effective as an oxidizer than oxygen and thermodynamically about 10^{10}× better at a temperature of 650 °C.
[19] Y. Krockenberger, J. Kurian, A. Winkler, A. Tsukada, M. Naito, and L. Alff, Phys. Rev. B **77**, 060505 (2008).
[20] S. J. Clark and J. Robertson, Appl. Phys. Lett. **94**, 022902 (2009).
[21] L. A. SEDER, Qual. Eng. **2**, 505 (1990).
[22] Rutherford scattering cross sections σ scale approximately as the atomic number squared Z^2 with computed σ values spanning 0.2 × 10^3 (oxygen, Z = 8), 1.8 × 10^3 (iron, Z = 26) and 17.7 × 10^3 mb/sr (bismuth, Z = 83). This scaling behavior reduces the sensitivity of the analysis to lighter elements. As a result, film oxygen concentrations are assigned nominal stoichiometric values. Furthermore, films with x = 0.90 and 1.07 exhibit rough surfaces that hinder accurate compositional quantification. Values reported for these layers are therefore estimated based on regression analyses carried out on the data shown in Fig. 1(a). The uncertainty of measured x values is ±0.07.
[23] I. Petrov, M. Braun, T. Fried, and H. E. Sätherblom, J. Appl. Phys. **54**, 1358 (1983).
[24] W. Eckstein and M. Mayer, Nucl. Instrum. Methods Phys. Res., Sect. B **153**, 337 (1999).
[25] J. F. Ihlefeld, A. Kumar, V. Gopalan, D. G. Schlom, Y. B. Chen, X. Q. Pan, T. Heeg, J. Schubert, X. Ke, P. Schiffer, J. Orenstein, L. W. Martin, Y. H. Chu, and R. Ramesh, Appl. Phys. Lett. **91**, 071922 (2007).
[26] J. F. Ihlefeld, N. J. Podraza, Z. K. Liu, R. C. Rai, X. Xu, T. Heeg, Y. B. Chen, J. Li, R. W. Collins, J. L. Musfeldt, X. Q. Pan, J. Schubert, R. Ramesh, and D. G. Schlom, Appl. Phys. Lett. **92**, 142908 (2008).
[27] J. F. Ihlefeld, W. Tian, Z.-K. Liu, W. A. Doolittle, M. Bernhagen, P. Reiche, R. Uecker, R. Ramesh, and D. G. Schlom, IEEE Trans. Ultrason., Ferroelectr., Freq. Control **56**, 1528 (2009).

[28]L. R. Dedon, S. Saremi, Z. Chen, A. R. Damodaran, B. A. Apgar, R. Gao, and L. W. Martin, Chem. Mater. **28**, 5952 (2016).
[29]The absolute uncertainty in measured out-of-plane lattice parameters is 0.0004 nm.
[30]A. K. Myers-Beaghton and D. D. Vvedensky, Phys. Rev. B **42**, 9720 (1990).
[31]J. Wollschläger, D. Erdös, and K. M. Schröder, Surf. Sci. **402-404**, 272 (1998).
[32]H. N. Lee, H. M. Christen, M. F. Chisholm, C. M. Rouleau, and D. H. Lowndes, Appl. Phys. Lett. **84**, 4107 (2004).
[33]F. Family and T. Vicsek, *Dynamics of Fractal Surfaces* (World Scientific, 1991).
[34]M. Volmer and A. Weber, Z. Phys. Chem. **119**, 227 (1925).
[35]S. Hasegawa, *Reflection High-Energy Electron Diffraction* (John Wiley & Sons, Inc., Hoboken, NJ, USA, 2002), Vol. 97.
[36]G. Ehrlich and F. G. Hudda, J. Chem. Phys. **44**, 1039 (1966).
[37]R. L. Schwoebel and E. J. Shipsey, J. Appl. Phys. **37**, 3682 (1966).
[38]Equilibrium polarization morphologies $\mathbf{u}(\mathbf{r})$ can be understood by minimizing a free energy functional comprised of three essential terms,

$$\mathcal{L}[\mathbf{u}(\mathbf{r})] = \int \mathcal{G}[\mathbf{u}(\mathbf{r})] + \mathcal{D}[\mathbf{u}(\mathbf{r})] + \mathcal{U}[\mathbf{u}(\mathbf{r})]d\mathbf{r},$$

where $\mathcal{G}[\mathbf{u}(\mathbf{r})] = |\nabla_{\mathbf{r}}\mathbf{u}(\mathbf{r})|^2$ represents the order parameter stiffness by associating an energetic cost with the magnitude of the field gradient $|\nabla_{\mathbf{r}}\mathbf{u}(\mathbf{r})|$,

$$\mathcal{D}[\mathbf{u}(\mathbf{r})] = \mathbf{u}(\mathbf{r}) \cdot \int (\nabla_{\mathbf{r}} \otimes \nabla_{\mathbf{r}'})G(\mathbf{r} - \mathbf{r}')\mathbf{u}(\mathbf{r}')d\mathbf{r}'$$

is a nonlocal dipole-dipole interaction which acts, through $G(\mathbf{r} - \mathbf{r}')$, the Green function of the Laplacian, to suppress stray $\mathbf{u}(\mathbf{r})$ fields, and $\mathcal{U}[\mathbf{u}(\mathbf{r})]$ is the potential energy function of the order parameter, describing crystalline anisotropy. The interplay between the order parameter stiffness, which penalizes the formation of domain walls, and the nonlocal interactions, which encourages the formation of domains, determines the equilibrium width of domains and, consequentially, the periodicity of ferroelectric domain patterns.
[39]C. Kittel, Phys. Rev. **70**, 965 (1946).
[40]C. Abert, G. Selke, B. Krüger, and A. Drews, IEEE Trans. Magn. **48**, 1105 (2012).
[41]G. A. Maugin, *Continuum Mechanics of Electromagnetic Solids* (Elsevier, 2013).
[42]J. Seidel, P. Maksymovych, Y. Batra, A. Katan, S. Y. Yang, Q. He, A. P. Baddorf, S. V. Kalinin, C. H. Yang, J. C. Yang, Y. H. Chu, E. K. H. Salje, H. Wormeester, M. Salmeron, and R. Ramesh, Phys. Rev. Lett. **105**, 197603 (2010).
[43]X. Qi, J. Dho, R. Tomov, M. G. Blamire, and J. L. MacManus-Driscoll, Appl. Phys. Lett. **86**, 062903 (2005).
[44]S. Saremi, R. Xu, L. R. Dedon, J. A. Mundy, S.-L. Hsu, Z. Chen, A. R. Damodaran, S. P. Chapman, J. T. Evans, and L. W. Martin, Adv. Mater. **28**, 10750 (2016).
[45]S. Saremi, R. Xu, L. R. Dedon, R. Gao, A. Ghosh, A. Dasgupta, and L. W. Martin, Adv. Mater. Interfaces **5**, 1700991 (2018).
[46]H. W. Jang, S. H. Baek, D. Ortiz, C. M. Folkman, C. B. Eom, Y. H. Chu, P. Shafer, R. Ramesh, V. Vaithyanathan, and D. G. Schlom, Appl. Phys. Lett. **92**, 062910 (2008).
[47]S. Saremi, R. Xu, F. I. Allen, J. Maher, J. C. Agar, R. Gao, P. Hosemann, and L. W. Martin, Phys. Rev. Mater. **2**, 084414 (2018).
[48]G. Le Rhun, G. Poullain, and R. Bouregba, J. Appl. Phys. **96**, 3876 (2004).
[49]Y. Zhou, X. Zou, L. You, R. Guo, Z. S. Lim, L. Chen, G. Yuan, and J. Wang, Appl. Phys. Lett. **104**, 012903 (2014).
[50]X. Zou, L. You, W. Chen, H. Ding, D. Wu, T. Wu, L. Chen, and J. Wang, ACS Nano **6**, 8997 (2012).
[51]S. Boyn, S. Girod, V. Garcia, S. Fusil, S. Xavier, C. Deranlot, H. Yamada, C. Carrétéro, E. Jacquet, M. Bibes, A. Barthélémy, and J. Grollier, Appl. Phys. Lett. **104**, 052909 (2014).
[52]R. Ramesh, W. K. Chan, B. Wilkens, H. Gilchrist, T. Sands, J. M. Tarascon, V. G. Keramidas, D. K. Fork, J. Lee, and A. Safari, Appl. Phys. Lett. **61**, 1537 (1992).